Supplementary Information

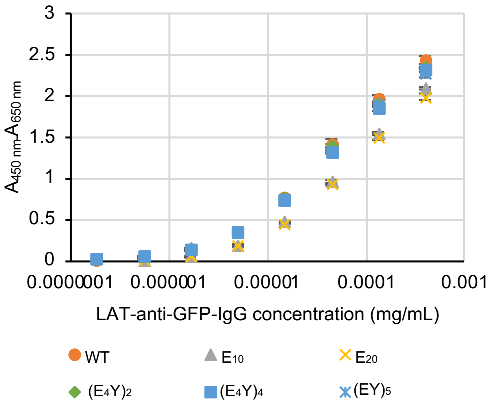

Supplementary Fig. 1. Evaluation of the binding ability of LAT-anti-GFP-IgG to EGFP using ELISA. EGFP fused with the nuclear localization signal sequence (NLS-EGFP) was immobilized, and the binding of LAT-anti-GFP-IgG was assessed using HRP-conjugated anti-mouse IgG. Error bars represent the mean ± standard error (SE) (*n* = 3).

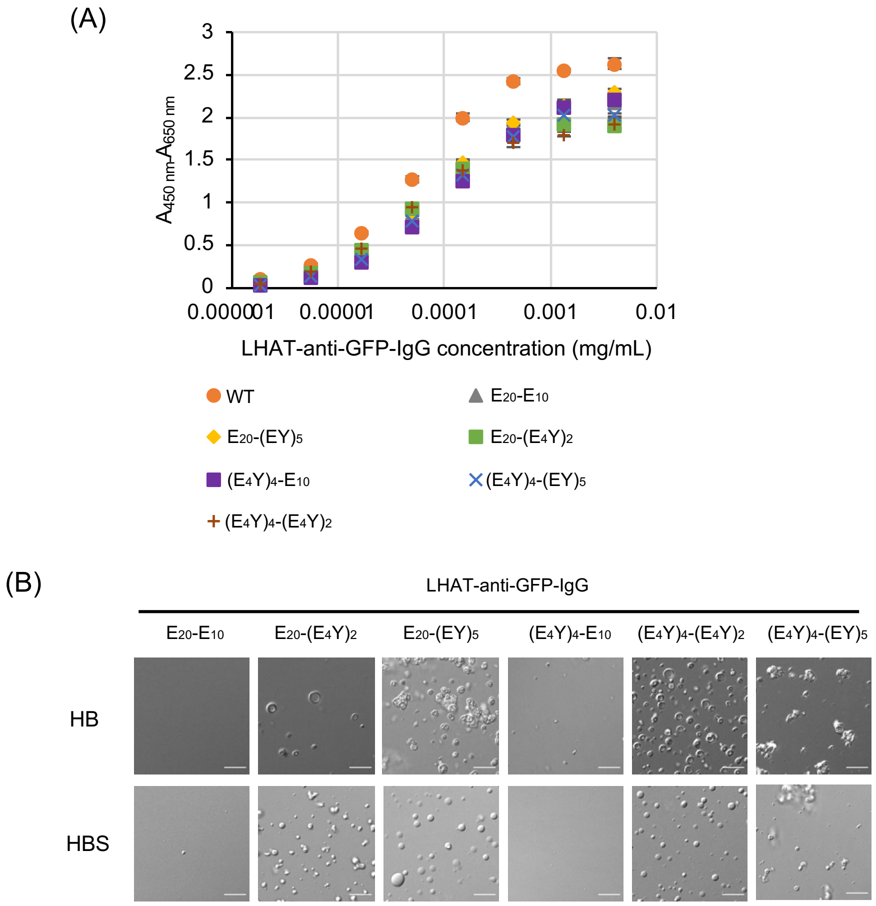

Supplementary Fig. 2. Evaluation of the target recognition ability of LHAT-anti-GFP-IgG and microcondensate formation in HB. (A) ELISA of LHAT-anti-GFP-IgG. The binding of LAT-anti-GFP-IgG to the immobilized NLS-EGFP was assessed using HRP-conjugated anti-mouse IgG. Error bars represent the mean ± SE (*n* = 3). (B) CLSM images of microcondensate formation by LHAT-anti-GFP-IgG and FcB(L17E)$_3$. (Upper panels) LAT-anti-GFP-IgG and FcB(L17E)$_3$ were incubated in HB for 30 min and diluted to yield the final concentration of 4 µM each as in Fig. 1E. LHAT-anti-GFP-IgG-E_{20}-$(E_4Y)_2$, LHAT-anti-GFP-IgG-E_{20}-$(EY)_5$, and LHAT-anti-GFP-IgG-$(E_4Y)_4$-$(EY)_5$ formed aggregates when incubated with FcB(L17E)$_3$. No remarkable condensate or aggregate structure was observed for the setup using LHAT-anti-GFP-IgG-E_{20}-E_{10} and LHAT-anti-GFP-IgG-$(E_4Y)_4$-E_{10}. (Lower panels) Considering that the attachment of peptide tags to the heavy chain of LAT-anti-GFP-IgG may enhance the interaction with FcB(L17E)$_3$, LHAT-anti-GFP-IgG and FcB(L17E)$_3$ were mixed in HBS directly to yield their final concentration of 4 µM (in Fig. 2F) in order to avoid possible aggregate formation due to excess interaction among them. However, similar tendencies were observed in microcondensate formation, as in Fig. 2F, even when LHAT-anti-GFP-IgGs and FcB(L17E)$_3$ were pre-incubated for 30 min in HBS at a higher concentration and diluted to yield the final concentration of 4 µM each (as in Fig. 1E). The scale bars represent 20 µm.

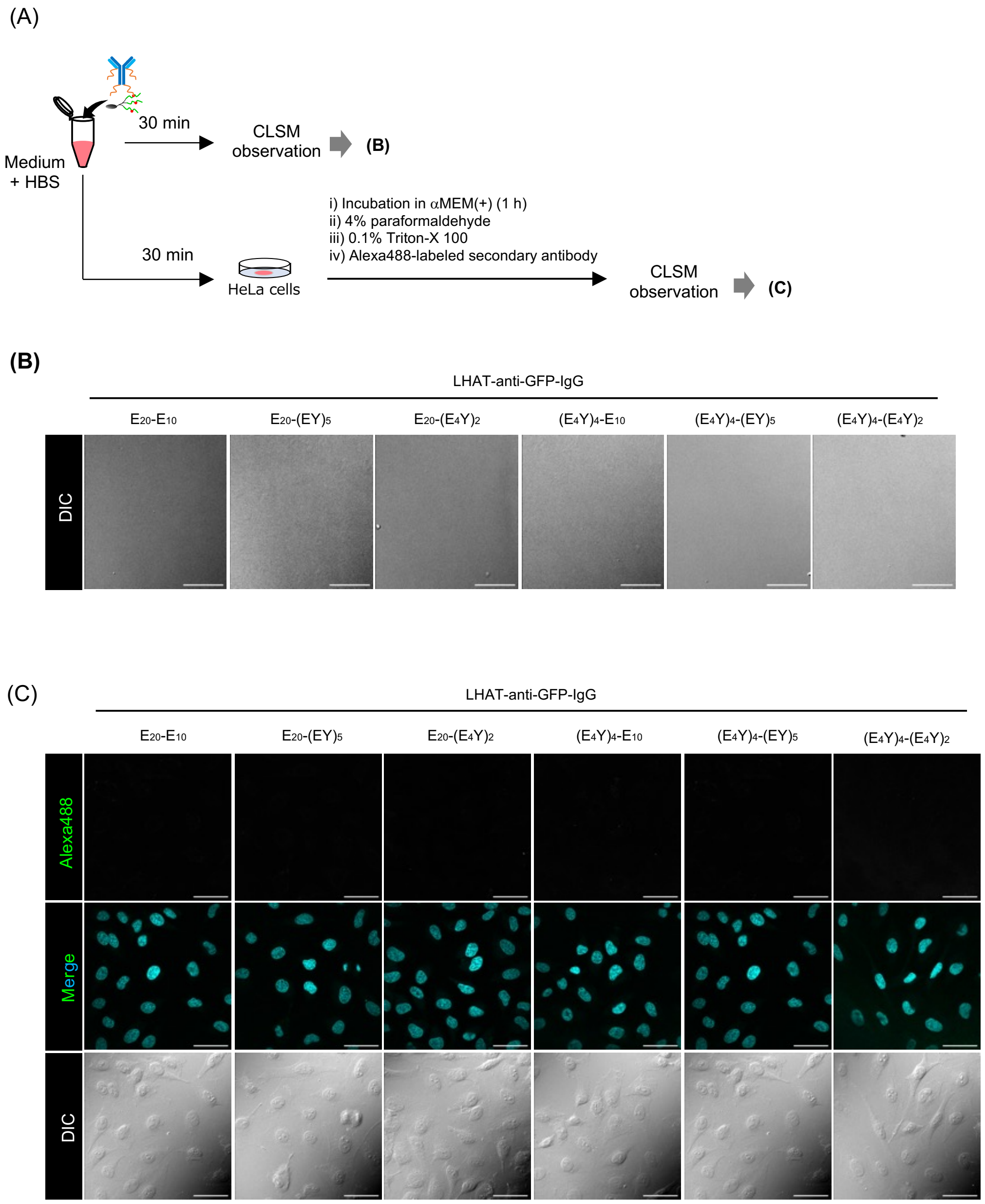

Supplementary Fig. 3. Addition of LHAT-anti-GFP-IgG and FcB(L17E)$_3$ without pre-incubation did not yield microcondensates and achieve cytosolic IgG delivery. (A) Experimental procedure for evaluating microcondensate formation and cytosolic IgG delivery after mixing LHAT-anti-GFP-IgG and FcB(L17E)$_3$ directly to yield their final concentration without pre-incubation. (B) Microscopic observation 1 hour after LHAT-anti-GFP-IgG and FcB(L17E)$_3$ were mixed to yield their final concentration (1 μM) in HBS:αMEM(+) (1:4). The scale bar represents 10 μm. (C) Representative confocal microscopic images of HeLa cells 1 hour after incubation with FcB(L17E)$_3$ and LHAT-anti-GFP-IgG, mixed without pre-incubation in HBS:αMEM(+) (1:4) and allowed to stand for 30 min, followed by immunostaining. The scale bars represent 50 μm.

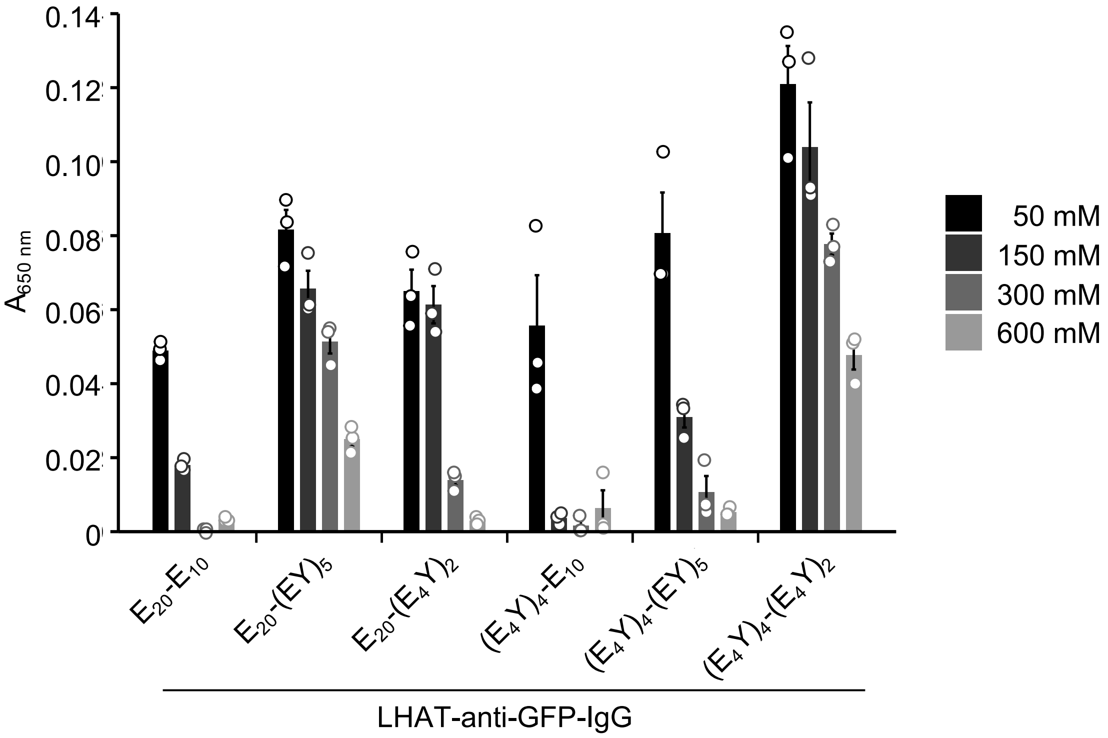

Supplementary Fig. 4. Turbidity assay of the microcondensates formed with LHAT-anti-GFP-IgGs and FcB(L17E)$_3$. FcB(L17E)$_3$ was mixed with each LHAT-anti-GFP-IgG followed by the addition of NaCl solution to yield the indicated final NaCl concentrations, and absorbance at 650 nm was measured. Error bars represent the mean ± SE (*n* = 3).

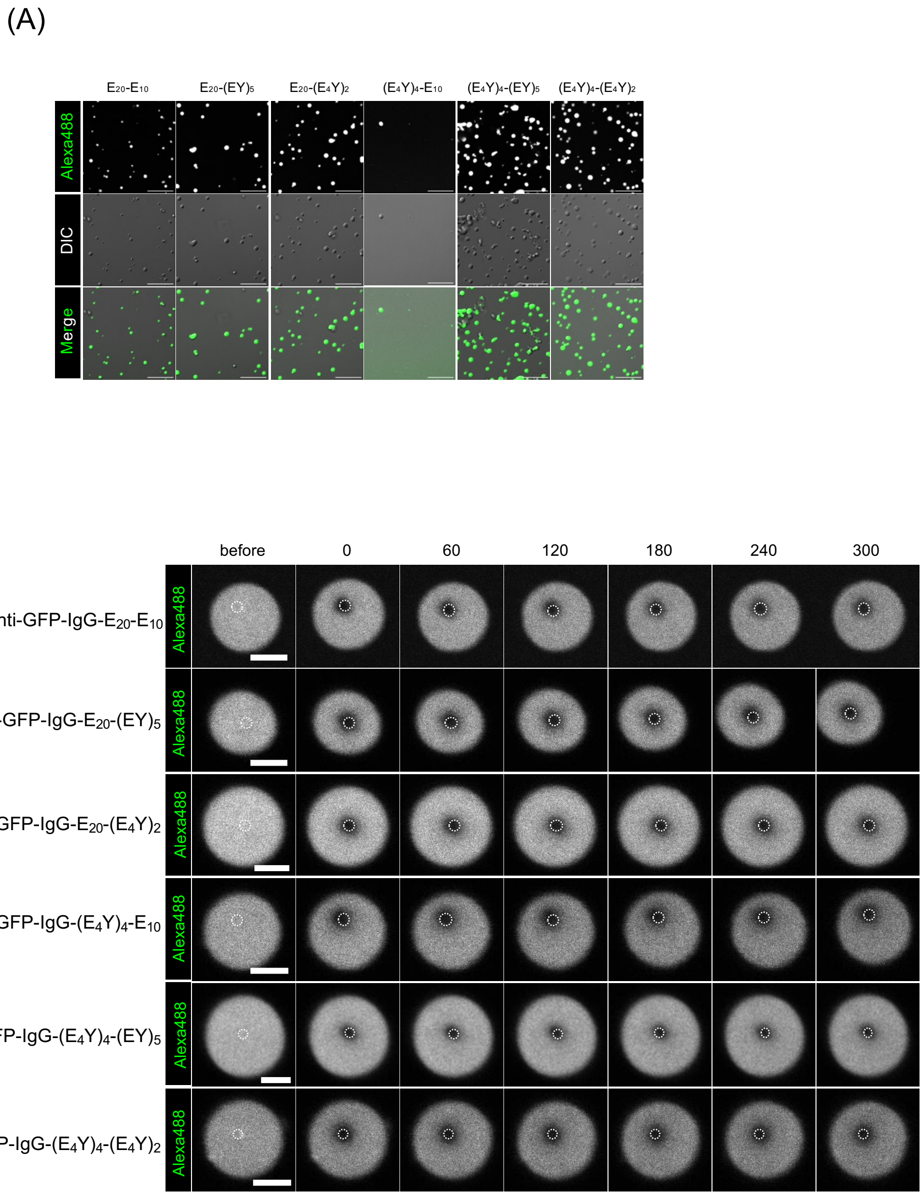

Supplementary Fig. 5. Fluorescence bleaching of microcondensates composed of LHAT-anti-GFP-IgG(Alexa488$_{part}$) and FcB(L17E)$_3$. (A) Confocal microscopy images of microcondensates composed of LHAT-anti-GFP-IgG(Alexa488$_{part}$) and FcB(L17E)$_3$. (B) Representative time-lapse confocal microscopy images of microcondensates composed of each LHAT-anti-GFP-IgG(Alexa488$_{part}$) with FcB(L17E)$_3$ before and after fluorescence bleaching. Scale bars represent 10 μm.

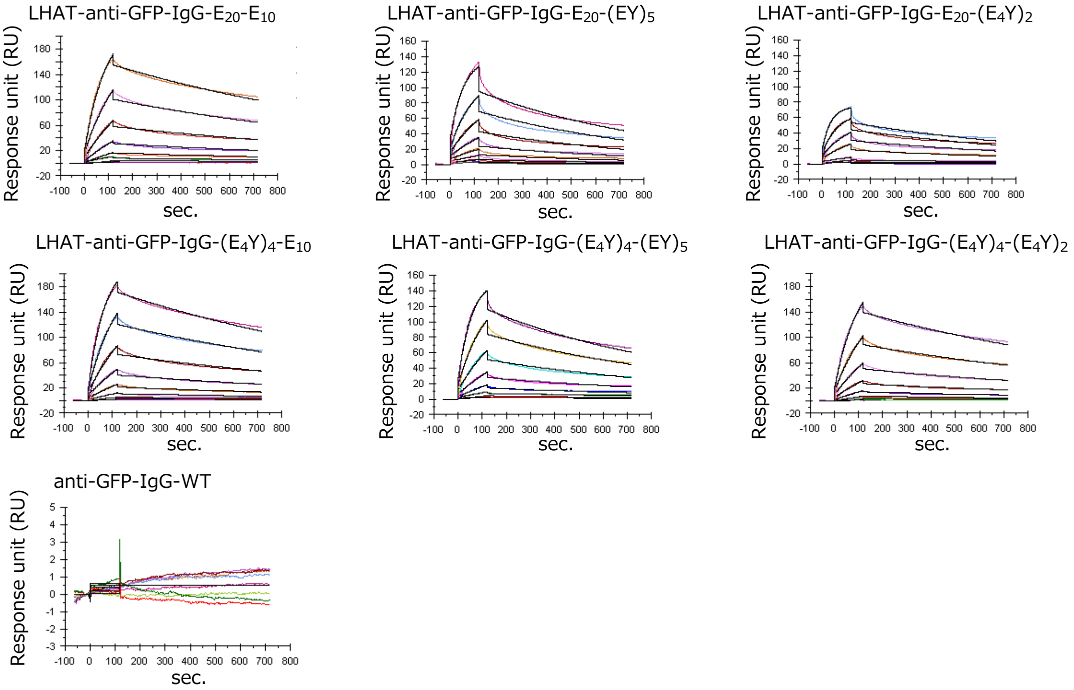

Supplementary Fig. 6. Binding analysis of LHAT-anti-GFP-IgGs with FcB(L17E)$_3$ using surface plasmon resonance. Sensorgrams were obtained by immobilizing biotin-modified FcB(L17E)$_3$ on an SA sensor chip.

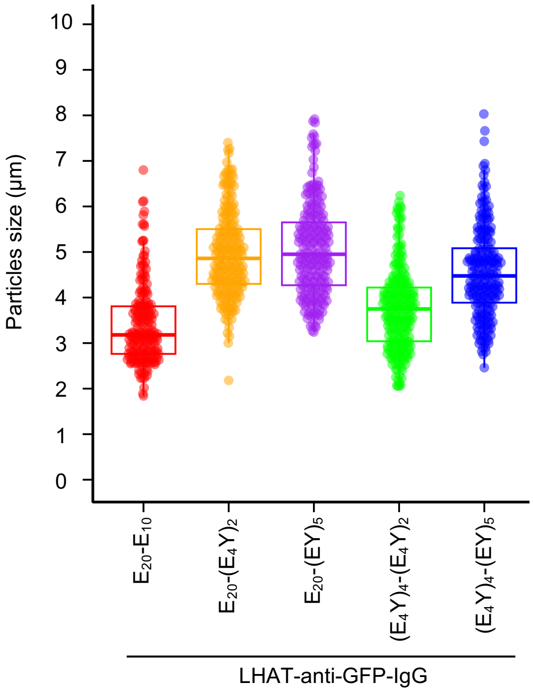

Supplementary Fig. 7. Particle size distribution of microcondensates. Dot plot of particle sizes of microcondensates composed of FcB(L17E)$_3$ and each LHAT-anti-GFP-IgG based on HT microscopic analysis. The median (horizontal bars) and first and third quartiles (boxes) for all analyzed values (circle) are shown.

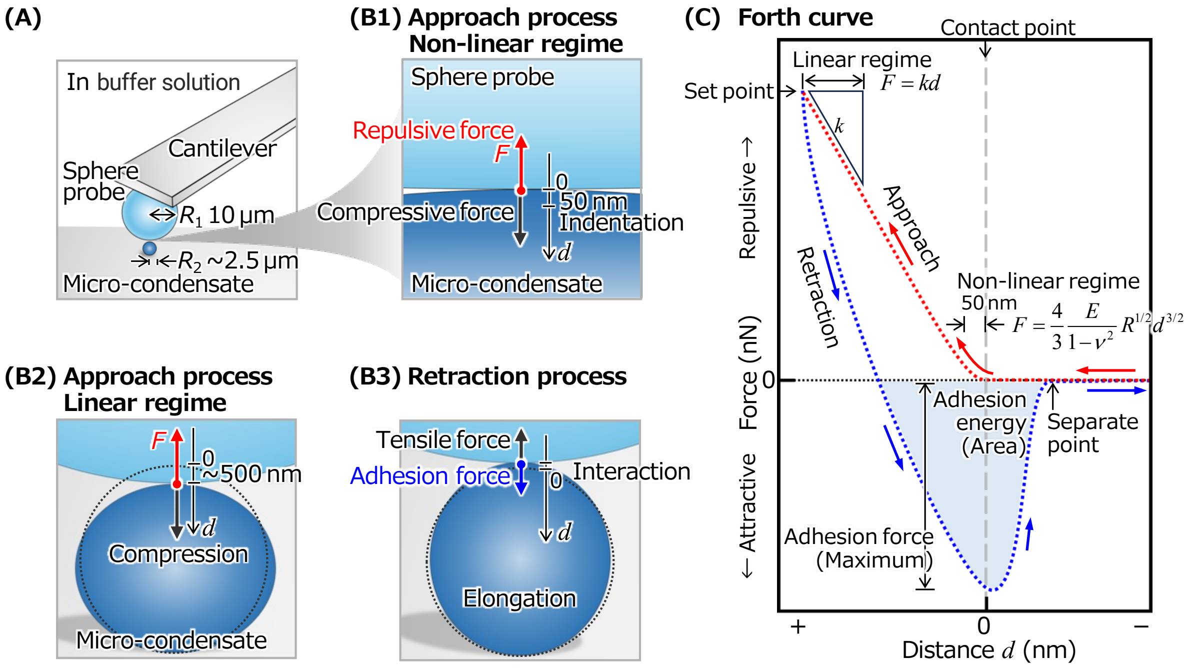

Supplementary Fig. 8. Schematic illustration of mechanical properties of the microcondensate. (A) The force spectroscopy system was used for measuring the force curve of the microcondensate. The silica particle with a radius (*R1*) 10 μm was attached to the AFM cantilever as the sphere probe. Each type of the microcondensate with an approximate radius (*R2*) 2.5 μm was settled on the bottom of the dish filled with a buffer solution. The ratio of the sizes (radius of curvature) of the sphere probe and the microcondensate and the distance (*d*) is accurately represented in the illustrations (A), (B1), (B2), and (B3). During (B1) the non-linear regime (*d* = 0 – 50 nm) and (B2) the linear regime (d = approximately 200 – 500 nm) in the approach process, the compressive force was applied, and the repulsive force was detected. Subsequently, in (B3) the retraction process, an interaction between the probe and the microcondensate caused adhesion, which caused an elongation. Each process or regime is indicated in (C) the schematic force curve. The Young's modulus (*E*) and stiffness (*k*) were estimated by fitting the approach force curve to equations (1) and (3), as indicated above the force curve. The adhesion force was measured as the maximum absolute value of the attractive force, and the adhesion energy was as an area filled with color.

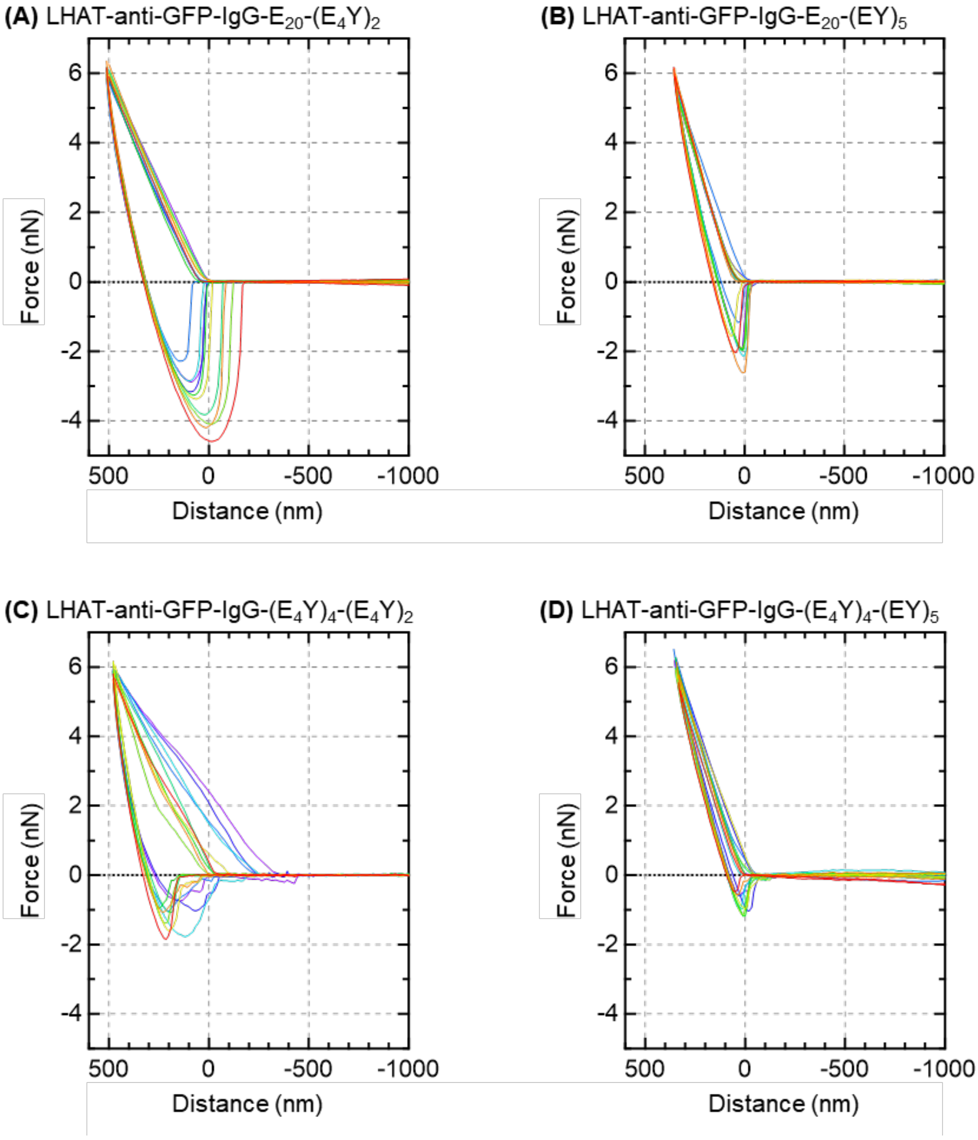

Supplementary Fig. 9. Force curves obtained by AFM. (A) During the approach phase of the silica bead to the microcondensate (red arrow), the probe was pressed into the microcondensate at a velocity of 5 µm/s. The region where the indentation distance *d* was 50 nm was defined as the Hertzian contact regime. The region up to an indentation of 500 nm was defined as the linear-elastic regime. The silica probe was pressed until the force (*F*) reached the set point of 6 nN, after which it was retracted from the microcondensate at a velocity of 5 µm/s; the retracting phase of the silica bead is shown with a blue arrow. Force curves of microcondensates containing (B) LHAT-anti-GFP-IgG-E_{20}-$(E_4Y)_2$, (C) LHAT-anti-GFP-IgG-E_{20}-$(EY)_5$, (D) LHAT-anti-GFP-IgG-$(E_4Y)_4$-$(E_4Y)_2$, and (E) LHAT-anti-GFP-IgG-$(E_4Y)_4$-$(EY)_5$ are shown. The distances were shifted to bring the minimum values to the same position for easy comparison of the slopes. Ten force curves were randomly selected from each data set and colored to see easily.

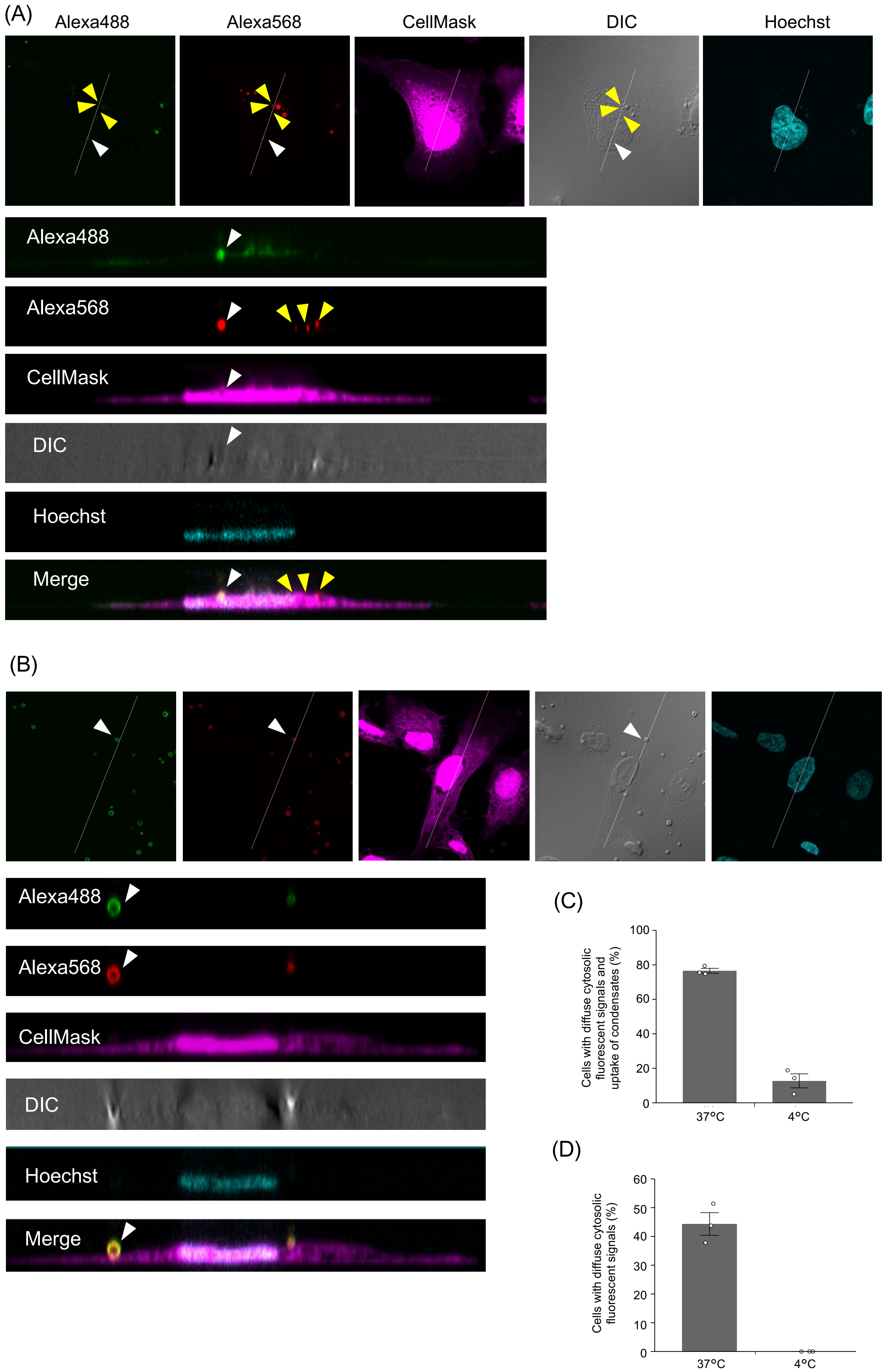
(A)
Alexa488
Alexa568
CellMask
DIC
Hoechst
Alexa488
Alexa568
CellMask
DIC
Hoechst
Merge
(B)
Alexa488
Alexa568
CellMask
DIC
Hoechst
Merge
(C)
Cells with diffuse cytosolic fluorescent signals and uptake of condensates (%)
100
80
60
40
20
0
37°C
4°C
(D)
Cells with diffuse cytosolic fluorescent signals (%)
60
50
40
30
20
10
0
37°C
4°C

Supplementary Fig. 10. Dual immunofluorescence after microcondensate treatment. (A, B) Confocal microscopy images of cells treated with microcondensate formed from LHAT-anti-GFP-E_{20}-$(E_4Y)_2$ and FcB(L17E)$_3$ at 37 °C (A) or 4 °C (B). The cell membrane and nucleus were stained with CellMask and Hoechst 33342, respectively, prior to performing the dual immunostaining using Alexa488- and Alexa568-labeled anti-mouse IgG. Panels at the top: x-y images; panels at the bottom: z-stack analysis along the white lines in the images on the top. (A) Images of the cells treated with the microcondensate formed from LHAT-anti-GFP-E_{20}-$(E_4Y)_2$ and FcB(L17E)$_3$ at 37 °C. The particle-like structure with the white arrowhead was stained by both Alexa488- and Alexa568-labeled anti-mouse IgG, suggesting that the particle stayed on the cell surface, which was further confirmed in the merged z-stack image. On the other hand, structures indicated by yellow arrowheads were only stained by Alexa568-labeled anti-mouse IgG, suggesting that the particle was only labeled after cell-membrane permeabilization by Triton-X 100. In the merged z-stack image, the Alexa568 was observed inside the cells. (B) Images of the cells treated with the microcondensate containing LHAT-anti-GFP-E_{20}-$(E_4Y)_2$ and FcB(L17E)$_3$ at 4 °C, where the ATP-dependent cellular machinery, including the actin restructuring and endocytosis, do not operate. Here, only the signals of Alexa568 overlapped with those of Alexa488 (white arrowhead), suggesting that the particle-like structure only stayed on cell surfaces without being internalized into cells. (C) The percentage of cells bearing either dot-like or diffuse Alexa568 signals and (D) that of cells having diffuse Alexa568 signals are shown.

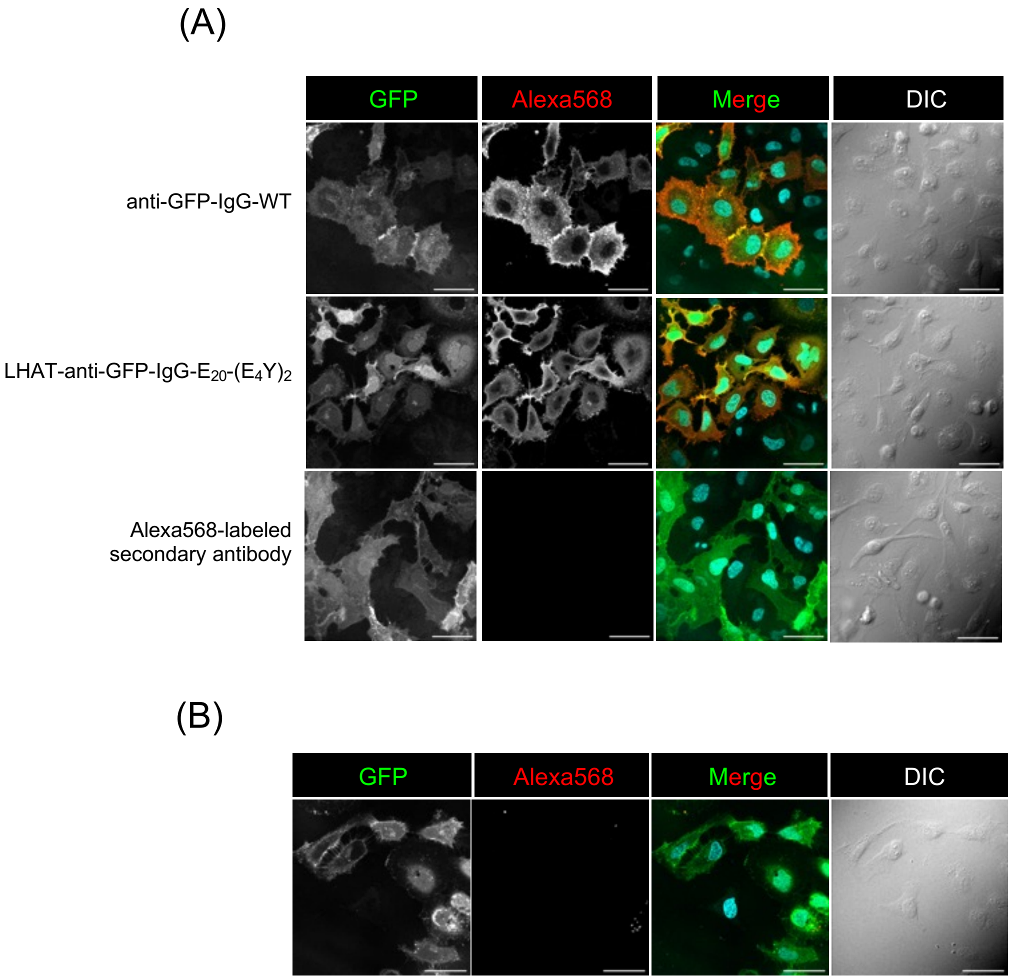

Supplementary Fig. 11. Antigen recognition capability of LHAT-anti-GFP-IgG. (A) Immunostaining of fixed and permeabilized HRas(G12V)-EGFP-expressing HeLa cells using wild-type anti-GFP-IgG (anti-GFP-IgG-WT) or LHAT-anti-GFP-IgG-E$_{20}$-(E$_4$Y)$_2$ as the primary antibodies. Fluorescence of Alexa568 was absent in cells not treated with primary antibodies (bottom) while colocalization of EGFP and Alexa568 was observed in cells treated with either anti-GFP-IgG-WT (top) or LHAT-anti-GFP-IgG-E$_{20}$-(E$_4$Y)$_2$ (middle), both showing patterns similar to those observed with wild-type anti-GFP-IgG. (B) Images of the cells treated with a mixture of anti-GFP-IgG-WT and FcB(L17E)$_3$ (as in Fig. S3).

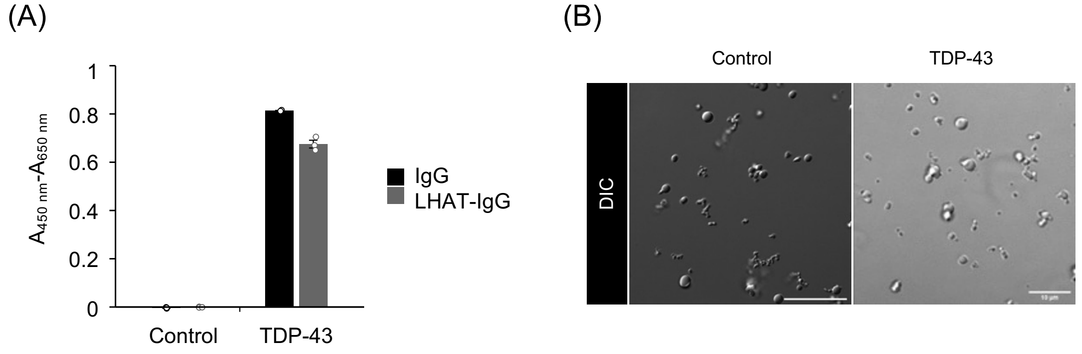

Supplementary Fig. 12. Evaluation of LHAT-anti-TDP-43-IgG binding and microcondensate formation. (A) ELISA of LHAT-anti-TDP-43-IgG-E_{20}-$(E_4Y)_2$. (Right) C-terminal domain of TDP-43, which is an intrinsically disordered region, was immobilized, and treated with anti-TDP-43-IgG without tag (black bar) and LHAT-anti-TDP-43-IgG-E_{20}-$(E_4Y)_2$ (shaded bar). The binding was evaluated using HRP-conjugated anti-human IgG. (Left) anti-pAkt-IgG without tag (black bar) and LHAT-anti-pAkt-IgG-E_{20}-$(E_4Y)_2$ (shaded bar) showed no binding to the C-terminal domain of TDP-43. Error bars represent the mean ± SE (*n* = 3). (B) Microscopy images of microcondensates formed by LHAT-anti-TDP-43-IgG-E_{20}-$(E_4Y)_2$ or LHAT-anti-pAkt-IgG-E_{20}-$(E_4Y)_2$ with FcB(L17E)$_3$ (TDP-43 or pAkt, respectively). The scale bars represent 20 μm.

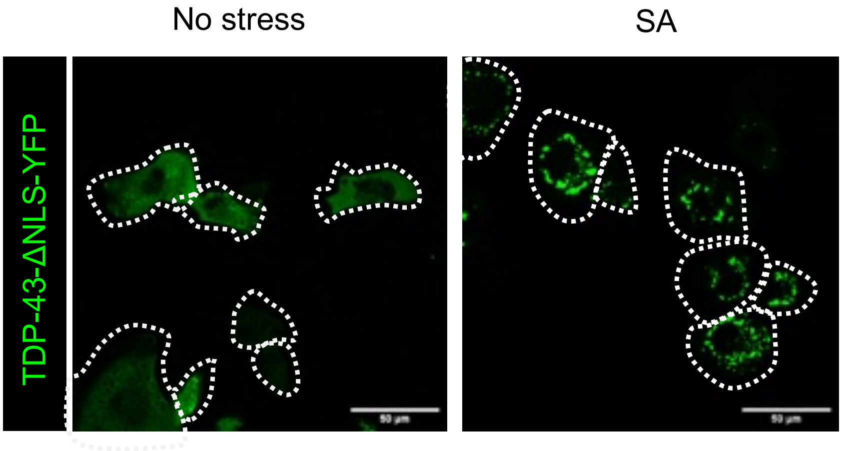

Supplementary Fig. 13. Stress granule formation in TDP-43ΔNLS-EYFP-expressing cells. TDP-43ΔNLS-EYFP-expressing HT1080 cells were treated with 500 μM sodium arsenite (SA) and observed by confocal microscopy 1 hour after treatment.

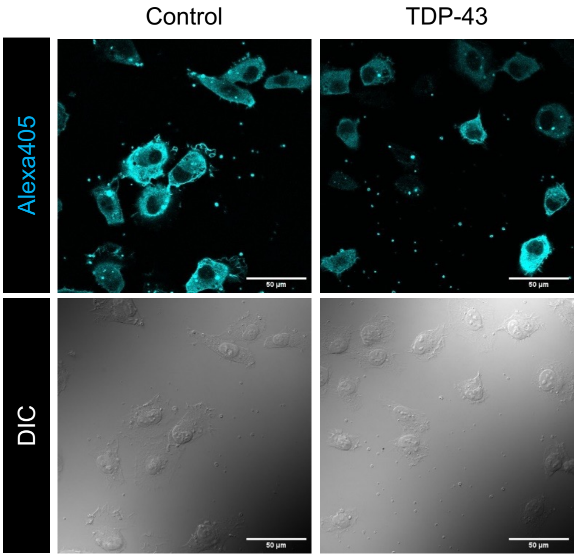

Supplementary Fig. 14. Cytosolic delivery of IgG by microcondensates formed by LHAT-anti-TDP-43-IgG-E_{20}-$(E_4Y)_2$. Representative confocal microscopy images of HT1080 cells treated with microcondensates, formed by mixing LHAT-anti-TDP-43-IgG-E_{20}-$(E_4Y)_2$ or LHAT-anti-pAkt-IgG-E_{20}-$(E_4Y)_2$ with FcB(L17E)$_3$, followed by immunostaining. The scale bars represent 50 µm.

Supplementary Table 1. Primer list.

antibody	domain	tag name	primer sequence (5’ → 3’)
anti-GFP-IgG	light chain	E_{10}	GCTTCAACAGGAATGAGTGTGAGGAGGAGGAAGAAGAGGAGGAGGAGGAGTACCCATACGATGTTCCAGATTACGCTTAGAGACAAAGGTCCTGAGA
		E_{20}	GCTTCAACAGGAATGAGTGTGAGGAGGAGGAAGAAGAGGAGGAGGAGGAGGAGGAAGAGGAGGAGGAGGAGGAGGAGTACCCATACGATGTTCCAGATTACGCTTAGAGACAAAGGTCCTGAGA
		$(E_4Y)_2$	GCTTCAACAGGAATGAGTGTGAGGAGGAGGAGTACGAGGAGGAGGAGTACTACCCATACGATGTTCCAGATTACGCTTAGAGACAAAGGTCCTGAGA
		$(E_4Y)_5$	GCTTCAACAGGAATGAGTGTGAGGAGGAGGAGTACGAGGAGGAGGAGTACGAGGAGGAAGAGTACGAGGAGGAGGAGTATTACCCATACGATGTTCCAGATTACGCTTAGAGACAAAGGTCCTGAGA
		$(EY)_5$	GCTTCAACAGGAATGAGTGTGAGTACGAGTACGAGTACGAGTACGAATACTACCCATACGATGTTCCAGATTACGCTTAGAGACAAAGGTCCTGAGA
		$(EY)_{10}$	GCTTCAACAGGAATGAGTGTGAGTACGAGTACGAGTACGAGTACGAATACGAATACGAGTACGAGTACGAGTACGAGTACTACCCATACGATGTTCCAGATTACGCTTAGAGACAAAGGTCCTGAGA
	heavy chain	E_{10}	CGGACTCCGGGTAAAGAGGAGGAAGAGGAGGAGGAGGAGGAGGACTACAAGGACGACGACGACAAGTGATCTAGACACGTG
		$(E_4Y)_2$	CGGACTCCGGGTAAAGAGGAGGAGGAGTACGAGGAGGAGGAGTACGACTACAAGGATGACGACGACAAGTGATCTAGACACGTG
		$(EY)_5$	CGGACTCCGGGTAAAGAGTACGAGTACGAGTACGAGTACGAGTACGACTACAAGGACGACGACGACAAGTGATCTAGACACGTG
anti-pAkt-IgG and antiTDP-43-IgG	light chain	E_{20}	CTTCAATAGGGGTGACTGTGAGGAGGAGGAAGAAGAGGAGGAGGAGGAGGAGGAAGAGGAGGAGGAGGAGGAGGAGTACCCATACGATGTTCCAGATTACGCTTAGCGGCCGCTATAAG
	heavy chain	$(E_4Y)_2$	CCATCTCCCGCTCTCCGGGTAAAGAGGAGGAGGAGTACGAGGAGGAGGAGTACGACTACAAGGATGACGACGACAAGTGAGCGGCCGCTCGAG